Liquid-Mediated Dense Integration of Graphene Materials for Compact Capacitive Energy Storage

Xiaowei Yang *et al.*

Science **341**, 534 (2013);
DOI: 10.1126/science.1239089

mesoporosity by a simple rinsing step with protic solvents like water or alcohols. It thus provides advantages over multiple-step fabrication methods currently used for integrating nanoscale porosity into macroscopic scaffolds. We have already shown it to work for different BCPs, small molar mass additives, solvents, and protic rinsing agents. Because the method is based on general thermodynamic principles, it may provide a powerful conceptual approach to generate hierarchical materials.

References and Notes

1. B.-L. Su, C. Sanchez, X.-Y. Yang, *Hierarchically Structured Porous Materials from Nanoscience to Catalysis, Separation, Optics, Energy, and Life Science* (Wiley-VCH, Weinheim, Germany, 2012).
2. I. W. Hamley, *The Physics of Block Copolymers* (Oxford Univ. Press, Oxford, 1998).
3. J. S. Lee, A. Hirao, S. Nakahama, *Macromolecules* **21**, 274–276 (1988).
4. A. M. Urbas, M. Maldovan, P. DeRege, E. L. Thomas, *Adv. Mater.* **14**, 1850–1853 (2002).
5. A. S. Zalusky, R. Olayo-Valles, J. H. Wolf, M. A. Hillmyer, *J. Am. Chem. Soc.* **124**, 12761–12773 (2002).
6. R. Mäki-Ontto *et al.*, *Adv. Mater.* **13**, 117–121 (2001).
7. Y. Wang, L. Tong, M. Steinhart, *ACS Nano* **5**, 1928–1938 (2011).
8. L. Li, X. Shen, S. W. Hong, R. C. Hayward, T. P. Russell, *Angew. Chem. Int. Ed.* **51**, 4089–4094 (2012).
9. S. Walheim, E. Schaffer, J. Mlynek, U. Steiner, *Science* **283**, 520–522 (1999).
10. D. A. Rider *et al.*, *Macromolecules* **41**, 2250–2259 (2008).
11. B. H. Jones, T. P. Lodge, *ACS Nano* **5**, 8914–8927 (2011).
12. W. Knoll *et al.*, *Small* **7**, 1384–1391 (2011).
13. K.-V. Peinemann, V. Abetz, P. F. W. Simon, *Nat. Mater.* **6**, 992–996 (2007).
14. K. Nakanishi, T. Amatani, S. Yano, T. Kodaira, *Chem. Mater.* **20**, 1108–1115 (2008).
15. W. A. Phillip *et al.*, *Nano Lett.* **11**, 2892–2900 (2011).
16. M. Seo, M. A. Amendt, M. A. Hillmyer, *Macromolecules* **44**, 9310–9318 (2011).
17. P.-G. d. Gennes, in *Scaling Concepts in Polymer Physics* (Cornell Univ. Press, Ithaca, NY, 1979), pp. 98–127.
18. F. S. Bates, *Science* **251**, 898–905 (1991).
19. K. L. Prime, G. M. Whitesides, *Science* **252**, 1164–1167 (1991).
20. W. R. Gombotz, W. Guanghui, T. A. Horbett, A. S. Hoffman, *J. Biomed. Mater. Res.* **25**, 1547–1562 (1991).
21. G. Floudas, R. Ulrich, U. Wiesner, *J. Chem. Phys.* **110**, 652 (1999).
22. See supplementary materials on *Science* Online.
23. J. S. Kasper, K. Lonsdale, *International Tables for X-Ray Crystallography* (Kynock, Birmingham, UK, 1952), vol. 2.
24. M. W. Matsen, F. S. Bates, *Macromolecules* **29**, 7641–7644 (1996).
25. F. J. Martinez-Veracoechea, F. A. Escobedo, *Macromolecules* **42**, 9058–9062 (2009).
26. F. J. Martinez-Veracoechea, F. A. Escobedo, *Macromolecules* **42**, 1775–1784 (2009).
27. T. C. Lee, R. L. Kashyap, C. N. Chu, *CVGIP Graphical Models Image Process.* **56**, 462–478 (1994).
28. A. S. Finnemore *et al.*, *Adv. Mater.* **21**, 3928–3932 (2009).
29. S. Koizumi, H. Hasegawa, T. Hashimoto, *Macromolecules* **27**, 6532–6540 (1994).
30. T. Ohta, A. Ito, *Phys. Rev. E* **52**, 5250–5260 (1995).

Acknowledgments: This work was supported by the NSF Single Investigator Award (DMR-1104773). K.W.T. gratefully acknowledges the Singapore Energy Innovation Programme Office for a National Research Foundation graduate fellowship. This work made use of the SEM, transmission EM, and polymer characterization facility of the Cornell Center for Materials Research (CCMR) with support from the NSF Materials Research Science and Engineering Centers (MRSEC) program (DMR-1120296) and CHESS, which is supported by the NSF and the NIH/National Institute of General Medical Sciences under NSF award DMR-0936384. This work also used the Xradia VERSA XRM-500 instrument in the Cornell University Biotechnology Resource Center (BRC) Multiscale CT Imaging Facility. The authors gratefully acknowledge S. Strogatz (Cornell University) for fruitful discussions; J. Song (Cornell University) for providing the triblock terpolymer; and R. Dorin, R. Li, and J. Kim (Cornell University) for experimental assistance and discussion.

Supplementary Materials

www.sciencemag.org/cgi/content/full/341/6145/530/DC1
Materials and Methods
Figs. S1 to S9
Table S1
References (*31*, *32*)
Movies S1 and S2

21 March 2013; accepted 25 June 2013
10.1126/science.1238159

Liquid-Mediated Dense Integration of Graphene Materials for Compact Capacitive Energy Storage

Xiaowei Yang, Chi Cheng, Yufei Wang, Ling Qiu, Dan Li*

Porous yet densely packed carbon electrodes with high ion-accessible surface area and low ion transport resistance are crucial to the realization of high-density electrochemical capacitive energy storage but have proved to be very challenging to produce. Taking advantage of chemically converted graphene's intrinsic microcorrugated two-dimensional configuration and self-assembly behavior, we show that such materials can be readily formed by capillary compression of adaptive graphene gel films in the presence of a nonvolatile liquid electrolyte. This simple soft approach enables subnanometer scale integration of graphene sheets with electrolytes to form highly compact carbon electrodes with a continuous ion transport network. Electrochemical capacitors based on the resulting films can obtain volumetric energy densities approaching 60 watt-hours per liter.

Electrochemical capacitors (ECs) store energy by charging electrical double layers through highly reversible ion adsorption on the surface of high-surface-area electrodes, generally made from porous carbon (*1*–*3*). They are attractive for energy storage because of their fast charging capability and long life span (*4*, *5*). The energy density (or the amount of energy stored per unit volume) of most commercially available ECs to date is close to 5 to 8 Wh/L (*6*), still much lower than that of lead-acid batteries (50 to 90 Wh/L) (*7*).

The efficiency of a material for EC energy storage can be described by its specific volumetric capacitance in a single electrode (C_{vol}) and energy density against the volume of two EC electrodes ($E_{vol\text{-}electrode}$); the volumetric energy density against the whole EC stack ($E_{vol\text{-}stack}$)—including two electrodes, electrolyte, a separator between two electrodes, and current collectors—was recently recommended to be a more reliable parameter than the gravimetric one to evaluate the real potential of a porous carbon for ECs (*8*–*10*). $E_{vol\text{-}stack}$ relates to gravimetric capacitance of the active carbon component in a single electrode ($C_{wt\text{-}C}$), packing density of the carbon (ρ), volume fraction of the electrodes in the device stack ($f_{electrode}$), as well as the nominal voltage (U) of the EC as follows (*6*).

$$C_{vol} = C_{wt\text{-}C} \times \rho \quad (1)$$

$$E_{vol\text{-}electrode} = \frac{C_{vol} \times U^2}{8} \quad (2)$$

$$E_{vol\text{-}stack} = E_{vol\text{-}electrode} \times f_{electrode} \quad (3)$$

Improvement in $E_{vol\text{-}stack}$ requires that $C_{wt\text{-}C}$, ρ, and $f_{electrode}$ of electrodes all be maximized, but increasing ρ and $f_{electrode}$ (or the thickness of electrodes) is difficult without substantially compromising the $C_{wt\text{-}C}$. As an example, graphite is possibly the most compact conductive carbon materials (~2.2 g/cm^3 at the ambient condition) but delivers little capacitance because ions cannot access the interplanar space. Even if the packing density of the graphene stack was reduced by half to 1.1 g/cm^3, the interplanar spacing would be only ~0.67 nm (fig. S1). The ion diffusion and adsorption in such small-size channels is very sensitive to pore size, surface wettability, and particularly the pore interconnectivity (*4*, *11*, *12*). Impaired ion transport in subnanometer pores becomes even more pronounced when the electrodes are made thicker, further limiting the achievable value of $E_{vol\text{-}stack}$ *(13, 14)*. Although progress has been made to achieve high $C_{wt\text{-}C}$ values through a variety of methods, such as laser scribing or chemical activation of graphene (*15*–*19*), the packing density

Department of Materials Engineering, Monash University, Clayton, VIC 3800, Australia.

*Corresponding author. E-mail: dan.li2@monash.edu

of the electrodes obtained was rather low, ranging from 0.05 to 0.75 g/cm^3 (*8*–*10*).

Recent advances in graphene chemistry (*20*, *21*), particularly the colloidal chemistry of chemically reduced graphene oxide (*22*), also called chemically converted graphene (CCG), open up new ways to address this challenge. We have shown that CCG can be well dispersed in water without the need for any surfactants by controlling its colloidal chemistry (*23*). The resulting CCG sheets, being microscopically corrugated (*22*), could self-assemble to form an oriented hydrogel film through a simple directional-flow–induced bottom-up assembly process (*24*). As a result of microcorrugation and repulsive intersheet solvation/electrostatic forces, CCG sheets in the hydrogel film remained largely separated, which gave rise to a high $C_{wt\text{-}C}$ of over 200 F/g (*25*). However, the as-formed gel film exhibited a low packing density (~0.069 g/cm^3), resulting in a mediocre C_{vol} (~18 F/cm^3).

In this work, we show that in contrast to porous carbon films prepared by the traditional techniques that generate fixed pore size and "hard" texture (*26*), the CCG hydrogel films, with a metastable and adaptive pore structure, can be compressed irreversibly by capillary pressure to increase the packing density through controlled removal of volatile solvent trapped in the gel. The graphene sheets in the films stacked in a nearly face-to-face fashion, so the packing density can be increased up to ~1.33 g/cm^3, nearly double that of the traditional activated porous carbon (0.5 to 0.7 g/cm^3) (*6*). More important, the liquid electrolyte-mediated CCG (EM-CCG) films created a continuous ion transport network that led to exceptionally high C_{vol} and $E_{vol\text{-}stack}$.

The CCG hydrogel films obtained by filtration of CCG dispersion were exchanged with a miscible mixture of volatile and nonvolatile liquids and were then subjected to removal of the volatile liquid by vacuum evaporation (fig. S2) (*27*). The gel film reduced in the thickness direction as a result of selective removal of the volatile liquid, while the CCG sheets remained solvated by the nonvolatile liquid during the whole process. The packing density of these flexible films (Fig. 1A) was controlled from 0.13 to 1.33 g/cm^3 by changing the ratio of volatile and nonvolatile liquids (Fig. 1D and fig. S9G). The nonvolatile liquid electrolytes, sulfuric acid, and 1-ethyl-3-methylimidazolium tetrafluoroborate (EMIMBF$_4$) were used in these studies.

Scanning electron microscopy (SEM) analysis revealed that the as-prepared EM-CCG films had a rather uniform cross section (Fig. 1, B and C, and figs. S3 and S9), which was also confirmed by energy dispersive x-ray spectroscopy (EDX) mapping of sulfur (fig. S3). The thicknesses were nearly proportional to the volumetric fraction of incorporated nonvolatile liquids trapped in the gels. X-ray diffraction (XRD) analysis showed that the as-compressed EM-CCG films displayed a nearly amorphous structure (fig. S4). Only a small and broad peak at around 23°, corresponding to a d_{002} distance of 0.39 nm, was detected when ρ > 0.76 g/cm^3 but the peak was much weaker than that of the dried CCG film. This indicated that the majority of CCG sheets did not restack back to graphite, despite being substantially compressed.

To investigate the effect of ρ on capacitive energy storage, we fabricated a series of prototype ECs with the same areal mass loading of CCG sheets (*27*). Fully dried CCG films with a ρ of 1.49 g/cm^3 were also tested for comparison. Figure 2 presents typical EC characterization of EM-CCG film–based ECs in 1.0 M H_2SO_4 electrolyte. The cyclic voltammetry (CV) curves (Fig. 2, A and B) showed nearly symmetrical rectangular shapes, indicative of an ideal capacitive behavior. As shown in Fig. 2C, a higher ρ led to a lower $C_{wt\text{-}C}$ at a given charging rate. However, the extent of decrease in capacitance was strongly dependent on whether the CCG film was preincorporated with an electrolyte during the preparation process of the film. At a low operation rate of 0.1 A/g, when ρ of the EM-CCG films was increased from 0.13 to 1.33 g/cm^3, $C_{wt\text{-}C}$ only dropped from 203.2 to 191.7 F/g (fig. S6A). In contrast, the completely dried CCG film (1.49 g/cm^3) only gave a $C_{wt\text{-}C}$ of 155.2 F/g. The difference became even more pronounced when the films were more rapidly charged (fig. S6, B to D). All of the EM-CCG films delivered a $C_{wt\text{-}C}$ > 100 F/g at an operation rate of 100 A/g, whereas the dried CCG film yielded only 10.2 F/g. The data obtained with an organic electrolyte [EMIMBF$_4$/acetonitrile (AN)] at an operation voltage of 3.5 V showed a similar result (figs. S10 and S11).

The influence of ρ on C_{vol} was very different. The C_{vol} of the EM-CCG films was nearly proportional to ρ (Fig. 2D and figs. S11E and S13). The highly compact EM-CCG films (1.25 to 1.33 g/cm^3) yielded a C_{vol} of 255.5 F/cm^3 in aqueous electrolyte and 261.3 F/cm^3 in organic electrolyte at 0.1 A/g. These values were much higher than those of the existing porous carbon materials (table S2). The EM-CCG films showed a very high C_{vol} at a broad range of charging rates from 0.1 (0.133 A/cm^3) to 200.0 A/g (266.0 A/cm^3). Even though the dried CCG film was able to deliver a C_{vol} of around 231.5 F/cm^3 at 0.1 A/g, the value decreased rapidly with the increase of operation rate (Fig. 2D) as a result of a rapidly declining $C_{wt\text{-}C}$.

The above results showed that preincorporation of electrolytes in the CCG films ensured excellent rate performance of compact EM-CCG films. We performed EC impedance spectroscopy analysis to further ascertain the role of the preincorporated electrolyte. A frequency response analysis at open circuit potential over the frequency

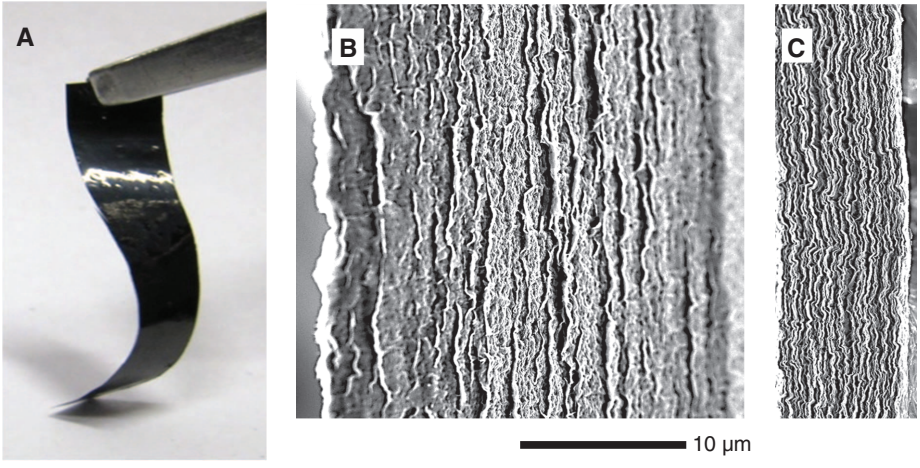

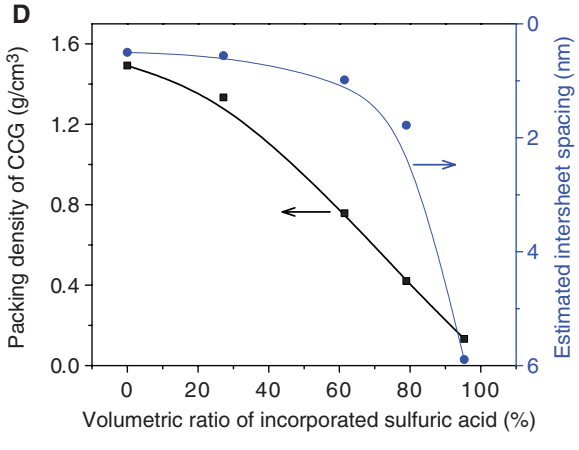

Fig. 1. Characterization of liquid electrolyte-mediated CCG (EM-CCG) films. (**A**) A photograph showing the flexibility of the film. (**B** and **C**) SEM images of cross sections of the obtained EM-CCG films containing (B) 78.9 volume percent (vol. %) and (C) 27.2 vol. % of H_2SO_4, respectively, corresponding to ρ = 0.42 g/cm^3 and ρ = 1.33 g/cm^3. (**D**) The relation between the volumetric ratio of incorporated electrolyte and the packing density as well as the estimated intersheet spacing.

range from 100 kHz to 10 mHz yielded the Nyquist plots shown in Fig. 2E. The plot featured a vertical curve, indicating a nearly ideal capacitive behavior of the cell. At high-frequency regions, a transition from a vertical curve feature to a –45° line followed by a semicircle was observed, and this transition was pushed to higher-frequency regions as a decrease in the packing density of EM-CCG film. This variation was small between the different EM-CCG films, but it showed a pronounced difference when they were compared with the dried one. The corresponding time constant τ_0 (the inverse of the characteristic frequency at which –45° is reached in the Bode phase plots) also responded in a similar fashion (Fig. 2F). The τ_0 increased from 0.51 to 0.73 s as the ρ of the EM-CCG films increased from 0.76 to 1.33 g/cm^3. A doubling of ρ only led to a change in τ_0 by a factor less than 1.45. By contrast, less than 20% change in ρ from the EM-CCG film (1.33 g/cm^3) to the dried film (1.49 g/cm^3) gave a shift of τ_0 by a factor more than 5.27. The frequency response of the CCG films in organic electrolyte followed a similar trend (fig. S10C).

The above results indicated that highly efficient ion transport channels were retained in the EM-CCG films, even when they were packed quite densely. Due to the fluid nature of liquid electrolytes, the continuous liquid network was likely to remain within the whole film during the capillary compression process. Furthermore, as the electrolyte became integrated within the film from the start of the assembly process, there was no subsequent wettability issue for these EM-CCG films, which remained a serious problem for the dried CCG film (*28*).

The indispensable role of the preincorporated electrolyte in ion transport was further evidenced by the effect of areal mass loadings (or electrode thickness) on the electrochemical performance (Fig. 3, A and B, and fig. S7). Both $C_{wt\text{-}C}$ and C_{vol} generally decreased with increasing thickness of the electrodes (*4*, *13*, *29*); this effect was particularly prominent when the pore size was in the subnanometer range (*13*). Figure 3 showed how the EC performance of the EM-CCG film (ρ = 1.25 g/cm^3) and the dried CCG film (ρ = 1.49 g/cm^3) responded to mass loading in the organic electrolyte. As with other porous carbon (*13*), both the C_{vol} and $E_{vol\text{-}electrode}$ of the two types of materials decreased with thickness. Nevertheless, the EM-CCG film displayed a much slower rate of decrease than the dried film, reflecting superior ion transport. When the effect

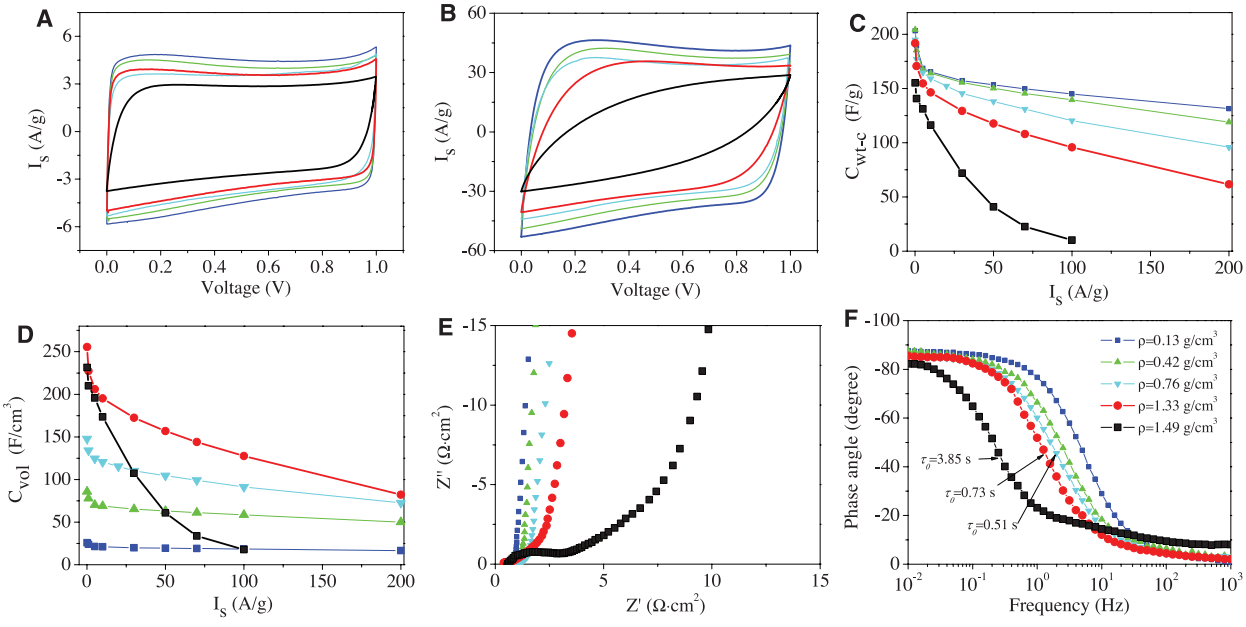

Fig. 2. Electrochemical characterization of EM-CCG films. Electrochemical characterization of EM-CCG films in 1.0 M H_2SO_4 (ρ = 0.13, 0.42, 0.76, and 1.33 g/cm^3, respectively). CV curves at (**A**) 50 mV/s and (**B**) 500 mV/s. (**C**) Gravimetric and (**D**) volumetric capacitances with varied charging/discharging current densities. (**E**) Nyquist plots and (**F**) Bode plots of phase angle versus frequency. The results for the dried CCG film (ρ = 1.49 g/cm^3) are also shown for comparison.

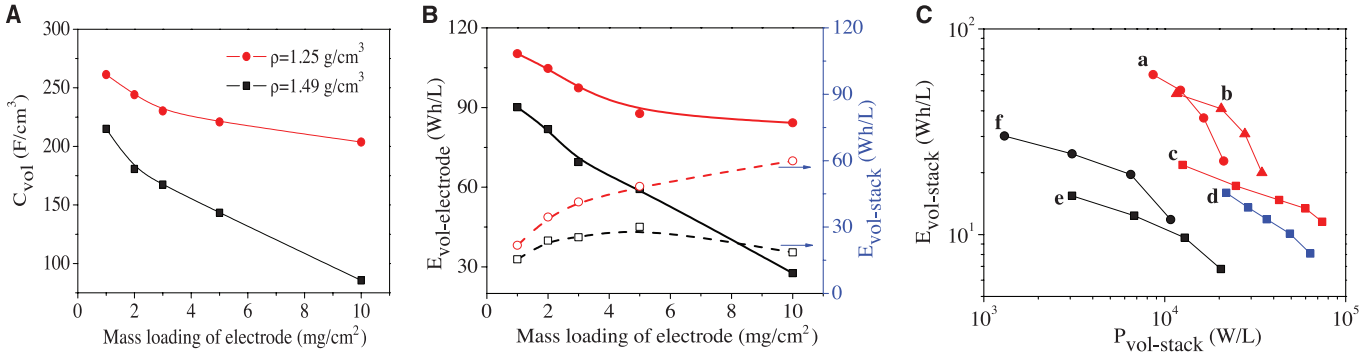

Fig. 3. Volumetric performance of ECs based on EM-CCG film electrodes. (**A**) Volumetric capacitance and (**B**) energy density as a function of the areal mass loading of EM-CCG film (ρ = 1.25 g/cm^3) and the dried CCG film (ρ = 1.49 g/cm^3) at the current density of 0.1 A/g. (**C**) Ragone plots of representative EM-CCG films showing how $E_{vol\text{-}stack}$ and $P_{vol\text{-}stack}$ depend on both the packing density and areal mass loading of CCG: (a) 1.25 g/cm^3, 10.0 mg/cm^2; (b) 1.25 g/cm^3, 5.0 mg/cm^2; (c) 1.25 g/cm^3, 1.0 mg/cm^2; (d) 0.39 g/cm^3, 1.0 mg/cm^2; the dried CCG films (1.49 g/cm^3) were also presented for comparison with the areal mass loading of (e) 1.0 mg/cm^2 and (f) 5.0 mg/cm^2. The data were obtained from the prototype ECs with $EMIMBF_4$/AN as electrolyte and an operation voltage of 3.5 V.

of thickness on $E_{vol\text{-}stack}$ was considered, the volume fraction of the active electrodes ($f_{electrode}$) needed to be taken into account (see Eq. 3). Because the $f_{electrode}$ increased with the electrode thickness and the other components of ECs remained unchanged, the reduction in $E_{vol\text{-}electrode}$ with thickness was not substantial in the case of the EM-CCG film; however, the EM-CCG film displayed an overall increase in $E_{vol\text{-}stack}$ with thickness (see the red dashed line in Fig. 3B). The EC device based on two CCG/electrolyte films of 80 μm (containing 10 mg/cm^2 of CCG, comparable to the amount of carbon contained in many commercial EC devices) yielded an $E_{vol\text{-}stack}$ of 59.9 Wh/L. By contrast, the $E_{vol\text{-}stack}$ of the dried CCG film initially increased with thickness, then decreased by a mass loading of 5 mg/cm^2 because of substantial drop in $E_{vol\text{-}electrode}$ (see the black dashed line in Fig. 3B). The maximum $E_{vol\text{-}stack}$ using 10 mg/cm^2 of the dried CCG film as electrodes was only ~18.4 Wh/L, further highlighting the crucial role of low ion transport resistance for achieving a high $E_{vol\text{-}stack}$.

The ECs based on our compact EM-CCG films also delivered a high volumetric power density. As shown in the Ragone plots (Fig. 3C), both the $E_{vol\text{-}stack}$ and the $P_{vol\text{-}stack}$ (maximum power density) were strongly dependent on the packing density and areal mass loading of CCG. The $P_{vol\text{-}stack}$ corresponding to the highest $E_{vol\text{-}stack}$ (59.9 Wh/L) was ~8.6 kW/L. With the same areal mass loading of 1 mg/cm^2, EM-CCG film (1.25 g/cm^3) could deliver the maximum power density of ~75 kW/L, higher than that of the dried CCG film (1.49 g/cm^3) as well as the low packing–density EM-CCG film (0.39 g/cm^3). These results also suggested that the key technical specifications of CCG-based ECs (e.g., $E_{vol\text{-}stack}$, $P_{vol\text{-}stack}$, and τ_0) could be readily customized to suit different applications by simply tuning the packing density of the CCG electrodes.

These EM-CCG films were very stable under repeated charging/discharging or under the application of a constant voltage (figs. S8 and S12). Over 95% of the initial capacitance was retained after a 300-hour constant voltage holding at 3.5 V in a neat $EMIMBF_4$ electrolyte (fig. S12). In addition, the fabrication of CCG gel films and subsequent compression are essentially compatible with the traditional cost-effective paper-making process and can be readily scaled up. All these attractive features make this class of graphene materials promising for large-scale real-world applications.

References and Notes

1. B. E. Conway, *Electrochemical Supercapacitors: Scientific Fundamentals and Technological Applications*, (Kluwer Academic/Plenum Publishers, New York, 1999).
2. J. R. Miller, *Science* **335**, 1312–1313 (2012).
3. P. Simon, Y. Gogotsi, *Nat. Mater.* **7**, 845–854 (2008).
4. A. G. Pandolfo, A. F. Hollenkamp, *J. Power Sources* **157**, 11–27 (2006).
5. J. R. Miller, P. Simon, *Science* **321**, 651–652 (2008).
6. A. Burke, *Electrochim. Acta* **53**, 1083–1091 (2007).
7. D. Linden, T. B. Reddy, *Handbook of Batteries, 3rd edition* (McGraw-Hill Publishers, New York, 2001).
8. Y. Gogotsi, P. Simon, *Science* **334**, 917–918 (2011).
9. S. Murali *et al.*, *Nano Energy* **2013**, 2013.01.007 (2013); http://dx.doi.org/10.1016/j.nanoen.2013.01.007.
10. P. Simon, Y. Gogotsi, *Acc. Chem. Res.* **46**, 1094–1103 (2013).
11. J. Maier, *Nat. Mater.* **4**, 805–815 (2005).
12. A. Izadi-Najafabadi, D. N. Futaba, S. Iijima, K. Hata, *J. Am. Chem. Soc.* **132**, 18017–18019 (2010).
13. J. Chmiola, C. Largeot, P. L. Taberna, P. Simon, Y. Gogotsi, *Science* **328**, 480–483 (2010).
14. V. Presser, M. Heon, Y. Gogotsi, *Adv. Funct. Mater.* **21**, 810–833 (2011).
15. M. D. Stoller, S. J. Park, Y. W. Zhu, J. H. An, R. S. Ruoff, *Nano Lett.* **8**, 3498–3502 (2008).
16. J. R. Miller, R. A. Outlaw, B. C. Holloway, *Science* **329**, 1637–1639 (2010).
17. Y. Zhu *et al.*, *Science* **332**, 1537–1541 (2011).
18. M. F. El-Kady, V. Strong, S. Dubin, R. B. Kaner, *Science* **335**, 1326–1330 (2012).
19. Y. Q. Sun, Q. O. Wu, G. Q. Shi, *Energy Environ. Sci.* **4**, 1113 (2011).
20. D. R. Dreyer, S. Park, C. W. Bielawski, R. S. Ruoff, *Chem. Soc. Rev.* **39**, 228–240 (2010).
21. M. J. Allen, V. C. Tung, R. B. Kaner, *Chem. Rev.* **110**, 132–145 (2010).
22. C. Cheng, D. Li, *Adv. Mater.* **25**, 13–30 (2013).
23. D. Li, M. B. Müller, S. Gilje, R. B. Kaner, G. G. Wallace, *Nat. Nanotechnol.* **3**, 101–105 (2008).
24. X. W. Yang *et al.*, *Angew. Chem. Int. Ed.* **50**, 7325–7328 (2011).
25. X. W. Yang, J. W. Zhu, L. Qiu, D. Li, *Adv. Mater.* **23**, 2833–2838 (2011).
26. C. Liu, F. Li, L. P. Ma, H. M. Cheng, *Adv. Mater.* **22**, E28–E62 (2010).
27. Materials and methods are available as supplementary materials on *Science* Online.
28. X. Huang, Z. Y. Zeng, Z. X. Fan, J. Q. Liu, H. Zhang, *Adv. Mater.* **24**, 5979–6004 (2012).
29. J. Y. Luo, H. D. Jang, J. X. Huang, *ACS Nano* **7**, 1464–1471 (2013).

Acknowledgments: The authors acknowledge the financial support from the Australian Research Council and G. P. Simon for helpful discussion. This work made use of the facilities at the Monash Centre for Electron Microscopy. D.L. and X.Y. filed an Australian provisional patent application (application no. 2013900820) on the basis of the work reported in this paper.

Supplementary Materials

www.sciencemag.org/cgi/content/full/341/6145/534/DC1
Materials and Methods
Figs. S1 to S13
Tables S1 and S2
References (*30*–*39*)

12 April 2013; accepted 28 June 2013
10.1126/science.1239089

Detection of a Spinning Object Using Light's Orbital Angular Momentum

Martin P. J. Lavery,[1]* Fiona C. Speirits,[2] Stephen M. Barnett,[2] Miles J. Padgett[1]

The linear Doppler shift is widely used to infer the velocity of approaching objects, but this shift does not detect rotation. By analyzing the orbital angular momentum of the light scattered from a spinning object, we observed a frequency shift proportional to product of the rotation frequency of the object and the orbital angular momentum of the light. This rotational frequency shift was still present when the angular momentum vector was parallel to the observation direction. The multiplicative enhancement of the frequency shift may have applications for the remote detection of rotating bodies in both terrestrial and astronomical settings.

The spin angular momentum of light is manifested as circular polarization and corresponds to the spin angular momentum of the photon, $\hbar$ (Planck's constant divided by 2π). More than 20 years ago, it was recognized that light beams with a helical phase structure described by $\exp(i\ell\phi)$, where ℓ is an integer and ϕ is the azimuthal coordinate, also carry an orbital angular momentum corresponding to $\ell\hbar$ per photon (*1*). Since then, this orbital angular momentum (OAM) has been studied in various contexts such as optical micromanipulation and quantum optics (*2*).

Consideration has been given to the use of OAM in imaging and remote sensing, where the detection of the angular momentum may reveal the structure or potentially the motion of the object (*3*–*7*). When light is scattered from a spinning object, we find that the rotation rate of the object can be measured by analyzing frequency shifts in the OAM of the light. This method of remote sensing has applications in both terrestrial and astronomical arenas.

The Doppler shift is a well-known phenomenon in which the relative velocity v between a wave-emitting source and an observer gives a frequency shift Δf of that wave. Such an effect is readily seen for audio waves, where the pitch of the sound changes with the speed of the source. For a light beam, the resulting frequency shift is $\Delta f = f_0 v/c$, where f_0 is the unshifted frequency and c is the speed of light. Less well-known than this linear effect is the rotational, or angular, Doppler effect (*8*–*11*). This frequency shift has also been considered for the scattering of light from atomic (*12*) or macroscopic (*13*) objects rotating around the axis of a helically phased laser beam. For a beam with helical phase fronts, a rotation of angular frequency

[1]School of Physics and Astronomy, Scottish Universities Physics Alliance (SUPA), University of Glasgow, Glasgow G12 8QQ, UK. [2]Department of Physics, SUPA, University of Strathclyde, Glasgow G4 ONG, UK.

*Corresponding author. E-mail: martin.lavery@glasgow.ac.uk